# The Commissioning of the Arcetri Near-Infrared Camera ARNICA: I. Characterization of the Detector

L. Hunt[1], R. Maiolino[2], and G. Moriondo[2]
Infrared Group

Arcetri Technical Report, N° 2/1994
Firenze, February 1994

[1] C.A.I.S.M.I.–C.N.R.
[2] Università degli Studi di Firenze

# Contents

# 1 Introduction

The Arcetri near-infrared (NIR) imaging camera ARNICA, first described in Lisi (1991), relies on a 256×256 HgCdTe array (NICMOS-3) developed by the Rockwell Corporation for the Hubble Space Telescope second generation instrumention. With respect to the NIR arrays previously available, the NICMOS-3 detector exhibits extremely low dark current ($\leq 5$ e$^-$ s$^{-1}$), low read noise ($\leq 50$ e$^-$), and high quantum efficiency (QE $\geq 65\%$ at $2\mu$m). Details of the optical and mechanical design of the camera are described in Lisi et al. (1993), and in an upcoming paper.

ARNICA saw first light at the TIRGO about one year ago, and both the camera and the data acquisition system (Baffa 1991) performed well from the start of the first commissioning campaign in November–December 1992. As a result, the first and subsequent commissioning runs of the camera have provided ample data by which to judge its astronomical performance. Tests performed at the telescope and in the laboratory have also enabled us to check the detector characteristics which were first measured in June, 1992, during the camera acceptance testing at Infrared Laboratories.

This report is the first of a series that describes the quantitative data analysis and the results obtained with ARNICA at the TIRGO during the commissioning of the camera (November 1992 – June 1993). The series of reports is based on broad-band data acquired in nineteen nights at the telescope (11 nights in December/January, 4 nights in February, and 4 nights in March), as well as data from laboratory tests. Presented here in the first report are the techniques used to characterize the detector and the derived parameters. In particular, we analyze detector performance in terms of: 1) conversion factor or gain; 2) read noise; 3) dark current; 4) non-linearity and its correction; and 5) cosmetic quality and the correction for bad pixels.

Future reports will describe the astronomical performance of the camera, techniques for data acquisition, the ARNICA data reduction package (available under IRAF), and first results from the NICMOS-3 photometric calibration program.

# 2 Brief description of array hardware

Although optical and NIR arrays appear similar to the observer, the physics and architecture behind their operation are different and the apparent similarity is a result of clever software. Optical CCDs are essentially analog shift registers composed of rows of tightly packed light-sensitive CMOS capacitors. During an exposure, photoelectrons are excited to the conduction band, then collected locally, automatically preserving the spatial distribution of the photon flux. During readout, the photoelectrons are transferred first across the image area, then down the store area to the output amplifier using the shift register feature of the CCD. Photon collection and the photoelectron readout are performed by the same Si array.

In contrast, infrared arrays in general, and NICMOS-3 arrays in particular, are hybrid devices in which the semiconductor array that collects the photons is distinct from the array that reads out the photoelectrons. The detector and the readout circuit arrays are fabricated separately, aligned, then bonded with small bumps of indium grown on each pixel to serve as the interface ("bump bonding"). The infrared array readout, known as a "Direct Read Out" multiplexer, reads out by sampling the voltage on the capacitances associated with individual pixels and decoding their (X,Y) address.

Before an exposure, the reset switch on each single multiplexer circuit is closed, and a reverse bias voltage is applied, charging the diode and readout circuit capacitance. During an exposure, the reset switch is opened (and the voltage may shift slightly), and the circuit capacitance is gradually discharged by the photocurrent that arises from the infrared photons impinging on the array. At any time during the exposure (but before the next reset), the multiplexer can measure the voltage across each capacitance. In this way, voltage can be read without changing its value ("non-destructive readout"), and many different readout algorithms can be used with multiplexed arrays (e.g., Fowler & Gatley 1990). The algorithm called double correlated sampling, implemented in ARNICA, is the simplest one that reduces the uncertainty in the voltage after the reset switch is opened ("kTC noise" + FET-induced injected charge) by reading out the array both *after* the reset and at the end of the elapsed exposure time *before* the next reset.

Optical and infrared arrays behave differently when exposed to extremely bright sources. Optical CCDs may exhibit "bleeding", in which charge from bright sources is not transferred completely during read-out, spilling over along a column to adjacent pixels. (This effect is eliminated in the modern high-quality devices.) While infrared arrays don't exhibit bleeding, they tend to have "memory" of bright sources; a series of array resets or short integrations may be required to eliminate the effects of sources at the saturation level of the array.

A more insidious difference between optical and infrared arrays from the observers' point of view is the inherent nonlinearity in the multiplexer readout of infrared hybrid arrays. While the CCD readout conserves almost everywhere and under almost all conditions the linear relationship between photoelectrons and output voltage, the multiplexer readout scheme does not. The capacitance of the readout circuit is not constant, but rather depends on the changing bias voltage as the capacitance is discharged during integration. This effect produces an intrinsic nonlinear relationship between the voltage sampled by the multiplexer and the photoelectrons collected by the detector. The effects of this are small ($\sim$ few percent) if operation is confined to well levels below the saturation level of the array, and can be corrected for empirically either during data acquisition or reduction. Analysis of the nonlinearity of the ARNICA NICMOS-3 array is discussed in §5.4, and a correction technique, although usually not necessary, is provided.

# 3 Test data acquisition

All of the results presented in this report were derived from data acquired in similar experimental setups: a spatially uniform, constant-illumination scene was imaged with the camera at a series of integration times. We used two different kinds of sources according to the parameter measured: illuminated sources for the conversion factor and effects of detector non-linearity, and zero-illumination sources for the read noise and dark current. The illuminated scenes were the inner surface of the dome at the telescope, and the pupil plane of the telescope simulator in the laboratory. Because of the large focal ratio of the telescope, irregular structures in the dome surface should be out of focus, and not greatly influence the spatial uniformity of the source. Zero flux levels were obtained with the dark slide of the camera inserted; these were repeated with each filter and with the cold stop at the camera pupil plane.

The temporal sequence for a series of measurements changed according to the derived parameter, that is according to the kind of source. For the measurements with illuminated sources, we wanted the instrumental counts (or ADUs, Analog-to-Digital Units) to range from 500 to 16000 ADUs, so we chose a series of exposure times to give counts in this range. Note that saturation occurs at roughly 16000 ADUs (corresponding to $\sim 3 \times 10^5 e^-$), instead of the more standard value for 15-bit analog-to-digital converters of 32767. The number of coadds[1] was fixed at 20 for short exposure times, and 15 for longer ones. We also experimented with fixed total times (i.e., fixed interval for the product coadds$\times$exposure time), so that the number of coadds changes with each exposure time. We found, however, that the variance determined from small numbers of frames is not reliable, and achieved more stable results with fixed numbers of coadds (at least 15 frames for each exposure time).

For the dark current measurements, the only requirement was that the integration times be sufficiently long as to adequately measure the extremely low dark current in these detectors. Typically at least 300 s were necessary for this. The number of coadds was as large as possible; ideally we used 15 or more.

The format for December and March measurements consisted of a set of coadds (15 or 20) for each of a series of integration times; we started with small integration times and ended with large ones. This data acquisition format samples the short-term temporal variations in the system response that are related to the stochastic behavior of the electronics and detector, which is what we want to measure for the derivation of the conversion factor and read noise. To monitor temporal stability of the source flux (to study the effects of non-linearity), a reference exposure time giving roughly 5000 ADUs was chosen and repeated with a fixed (10) number of coadds. The set of reference integrations was repeated before and after each different exposure time. This data acquisition scheme is indicated by the superscript $a$ in the following tables.

The format for the June laboratory measurements consisted of a series of integration times repeated 15 or 20 times to acquire a sufficient set of coadds. This format obviates the need for reference frames, since each frame is rescaled to a common

[1] Coadds are the number of homologous images to be added together for a given exposure time.

Table 1: ARNICA characterization tests.

| Date | Code Name | Source | Filter | Range in $t_{int}$ [s] | Range in ADU |
|---|---|---|---|---|---|
| 28 Oct 92[a] | – | Dark | D | 60, 300, 600 | 5 – 15 |
| 8 Dec 92[a] | Linear1 | Illumin. | K | 4 – 40 | 1500 – 16000 |
| 10 Dec 92[a] | – | Dark | D | 10 – 600 | 5– 15 |
| 10 Dec 92[a] | Linear3 | Illumin. | K | 3 – 20 | 2500 – 17500 |
| 15 Mar 93[a] | Linear5 | Illumin. | K | 1 – 39 | 400 – 16300 |
| 1 Jun 93[b] | Linear6 | Illumin. | J | 1 – 25 | 450 – 12900 |
| 1 Jun 93[b] | Linear7 | Illumin. | H | 1 – 25 | 400 – 10600 |
| 1 Jun 93[b] | Linear8 | Illumin. | J | 1 – 39 | 250 – 10600 |
| 1 Jun 93[b] | Linear9 | Illumin. | H | 1 – 39 | 250 – 11500 |
| 3 Jun 93[b] | – | Dark | D | 2 – 30 | 3 – 7 |
| 14 Jun 93[b] | – | Dark | H | 10 – 100 | 5 – 11 |
| 15 Jun 93[b] | – | Dark | J | 10 – 100 | 5 – 9 |
| 16 Jun 93[b] | – | Dark | K | 10 – 100 | 6 – 19 |

Notes to Table 1:

[a] Repeated $\forall i$: $[N_{\rm coadds} \times t_{\rm int}(i) + N_{\rm coadds} \times t_{\rm ref}]$.

[b] Repeated $\forall N_{\rm coadds}$: $\{\forall i: \ [1 \times t_{\rm int}(i)]\}$.

median during the image combining. Moreover, human intervention is minimized as this form of measurement is an option in the data acquisition program. On the other hand, the short-term temporal variations that define the noise characteristics of the system (e.g., the read noise) are not well-sampled. This data acquisition scheme is indicated by the superscript $b$ in the following tables. A log of all of the measurements used in this report is given in Table 1.

# 4 Data analysis

Two kinds of representations are necessary to derive the detector parameters. One is signal vs. exposure time in which detector spatial trends are considered, and the other is variance vs. signal in which detector spatial trends can be ignored. When the dark current measurements are represented as signal vs. exposure time, we can calculate dark current levels by performing linear pixel-by-pixel fits. When illuminated source measurements are thus represented, we can calculate the effects of non-linearity.

The 'variance' or 'photon transfer' method relies on the second representation, or variance vs. signal, to derive the gain factor $g$ and the read noise $\sigma_r$ (e.g., Mackay 1986; McLean 1988). This method exploits the theoretical form for the scatter of a series of identical measurements around their mean. The scatter or noise should be entirely due to two noise sources: 1) photon noise from the photoelectrons; and 2) read noise from the detector amplifiers. The total variance of the signal in a series of measurements is then the sum of these two contributions added in quadrature. As long as the noise is adequately described by these two components, there will be a series of different noise regimes as the signal varies. At low signals as in those for dark current exposures, the variance is roughly constant; as the signal increases, a straight line will theoretically describe the variance as a function of signal. At high signals, the variance again levels off because of the onset of satuation. The intercept of the plot at zero signal is equal to the read noise squared in units of ADUs. In the linear regime, the slope is the inverse of the gain or conversion factor $1/g$, where the units of $g$ are $e^-$/ADU.

The read noise can be calculated either from dark current measurements or from illuminated source frames, although the dark current measurements give a more accurate estimate of the noise associated with the reading out of the detector. The gain factor can be calculated only from the illuminated source frames as there is not enough dynamic range in the dark current measurements to be able measure signal-dependent variance.

## 4.1 Signal vs. exposure time

As described above, each test consists of a set of frames at each of a series of exposure times. For the analysis of detector dark current and non-linearity, we are interested in spatial variations and thus must consider the detector on a pixel-by-pixel basis. By averaging small areas together, we can increase signal-to-noise at the expense of spatial resolution, although generally this provides only a check on the pixel-by-pixel results.

We determined a median image from the set of frames at a given exposure time by calculating scaled (to the image median) stack medians for each pixel. When fixed-exposure time sets were interspersed throughout the series of exposure times, we were able to explicitly determine the temporal variation of the illumination level. The average of the frame median was calculated for each pair of fixed-exposure time sets and, when necessary, a constant rescaling (ratio of the pair to the global average) was applied.

The median images were then fit, pixel-by-pixel, to first- (dark current) or second-order (non-linearity) polynomials as a function of exposure time. Linear or first-order fits give an image of a time-independent offset and an image of the mean flux per pixel per unit time; quadratic or second-order fits give an additional image of the lowest-order deviation from linearity.

## 4.2 Variance vs. signal

For each exposure time, we calculated a median image as described above. We also calculated a scaled (to the image median) stack mean for each pixel and the standard deviation of the set of frames around the stack mean. This was then squared to form the variance frame. We noticed that the values obtained for gain factor and read noise change systematically according to the kind of combination algorithm we used. In particular, scaling the individual images to the image median before combining them reduces the variance associated with each group and, more importantly, increases the signal-to-noise of the fitting procedure.

Because spatial variations within a detector quadrant[2] can in principle be ignored in the calculation of read noise and gain factor, we chose to increase signal-to-noise by averaging together small spatial areas. This was done by calculating spatial medians of subareas in the variance and the median images; we chose areas of 16×16 pixels as a compromise between signal-to-noise and the typical scalelength of spatial variations in the detector quantum efficiency (QE). For each subarea, we derived a pair of numbers, that is the spatial median of the stack variance and the spatial median of the stack (scaled) median. These pairs, organized into quadrants, were submitted to a first-order linear regression, omitting signal values exceeding 10000 ADU to avoid effects of saturation in signal level. The intercept of this regression is the square of the read noise (in ADU) and the slope is the inverse of the gain factor (in $e^-$/ADU).

# 5 Results

The test images were used to measure the conversion or gain factor, read noise, dark current, detector non-linearity, and to derive a bad pixel mask.

## 5.1 Conversion or gain factor

The images from an illuminated source at a series of integration times were converted into the variance vs. signal representation as described in §4.2. Figures 1 – 3 show examples of data acquired in December (1992), March, and June (1993). Values from individual subareas are organized into detector rows (in the figure referred to as lines); only one quadrant is shown. The onset of saturation can be seen from the figures, as the variance tends to decrease at high signal levels. The dotted lines are the quadrant fits described in the next paragraph.

For the analysis, the subareas were grouped into quadrants and a linear regression was performed on the spatial medians of the stack variance relative to the stack median. The results of these fits, based on typically 600 – 800 data points (i.e., the product of 64 subareas per quadrant and the number of exposure times in the test sequence with signal $\leq$ 10000), are shown in Table 2. Units are $e^-$/ADU.

Analysis shows that we can safely assume a gain or conversion factor of 19.9–20.0$e^-$/ADU for the ARNICA array. The gain appears to be constant over time, certainly over the six month period spanned by the tests, as the array averages are the same to within the errors. Quadrant variation seems to be negligible, as the differences between a single quadrant and the mean are significant only at $2\sigma$.

[2]NICMOS-3 arrays are read out by quadrant with independent electronic circuitry for each quadrant.

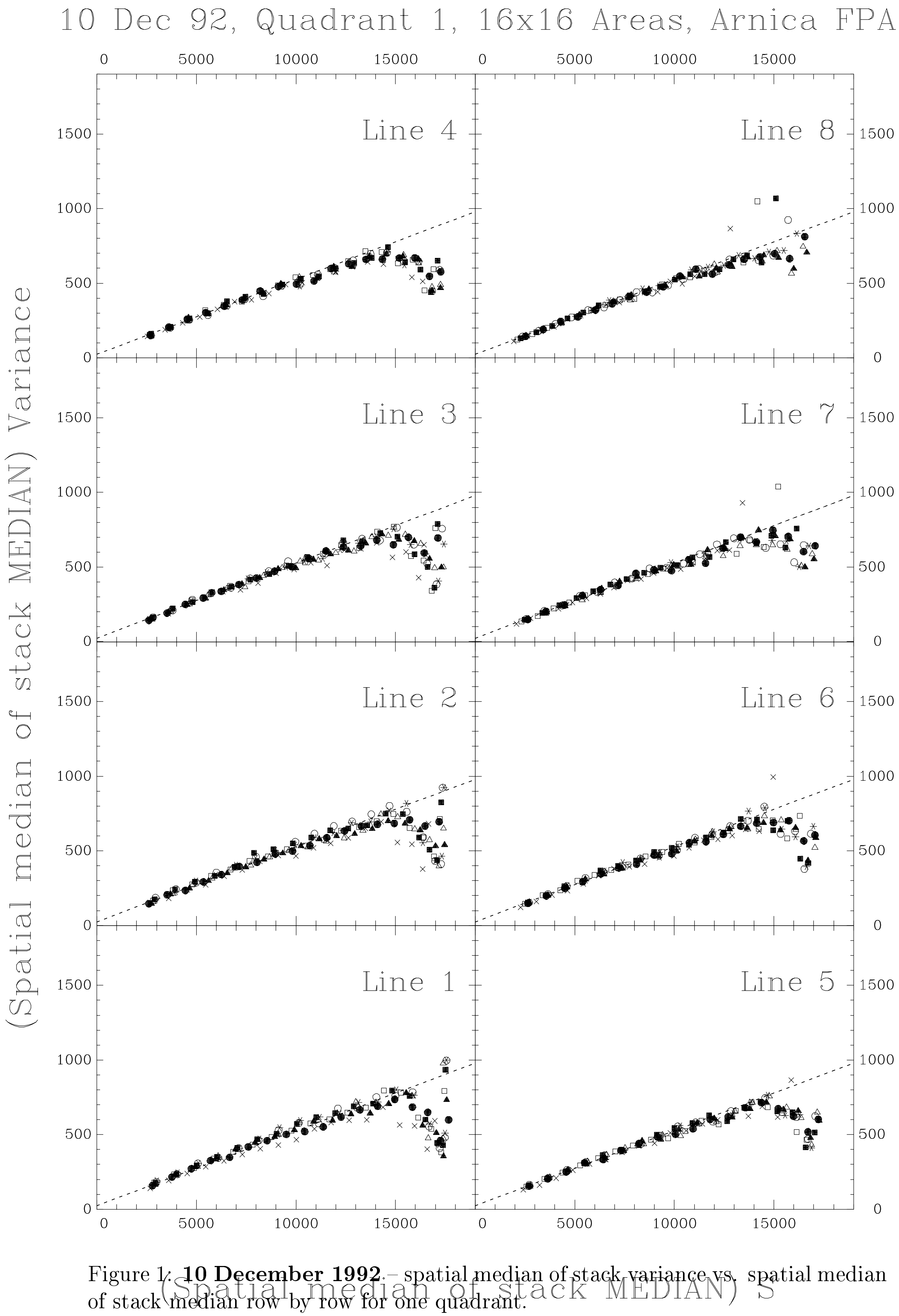


Figure 1: **10 December 1992** – spatial median of stack variance vs. spatial median of stack median row by row for one quadrant.

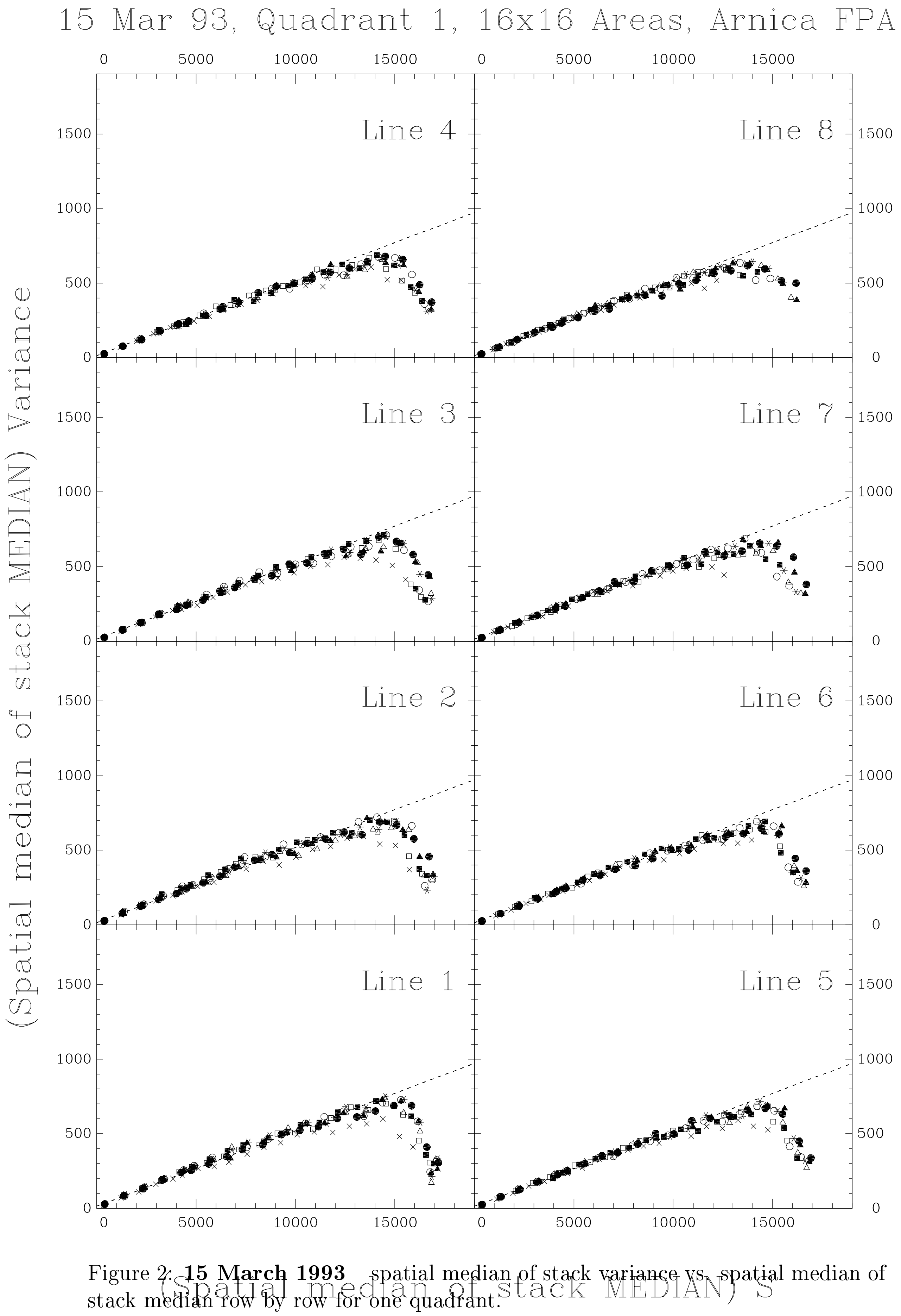


Figure 2: **15 March 1993** – spatial median of stack variance vs. spatial median of stack median row by row for one quadrant.

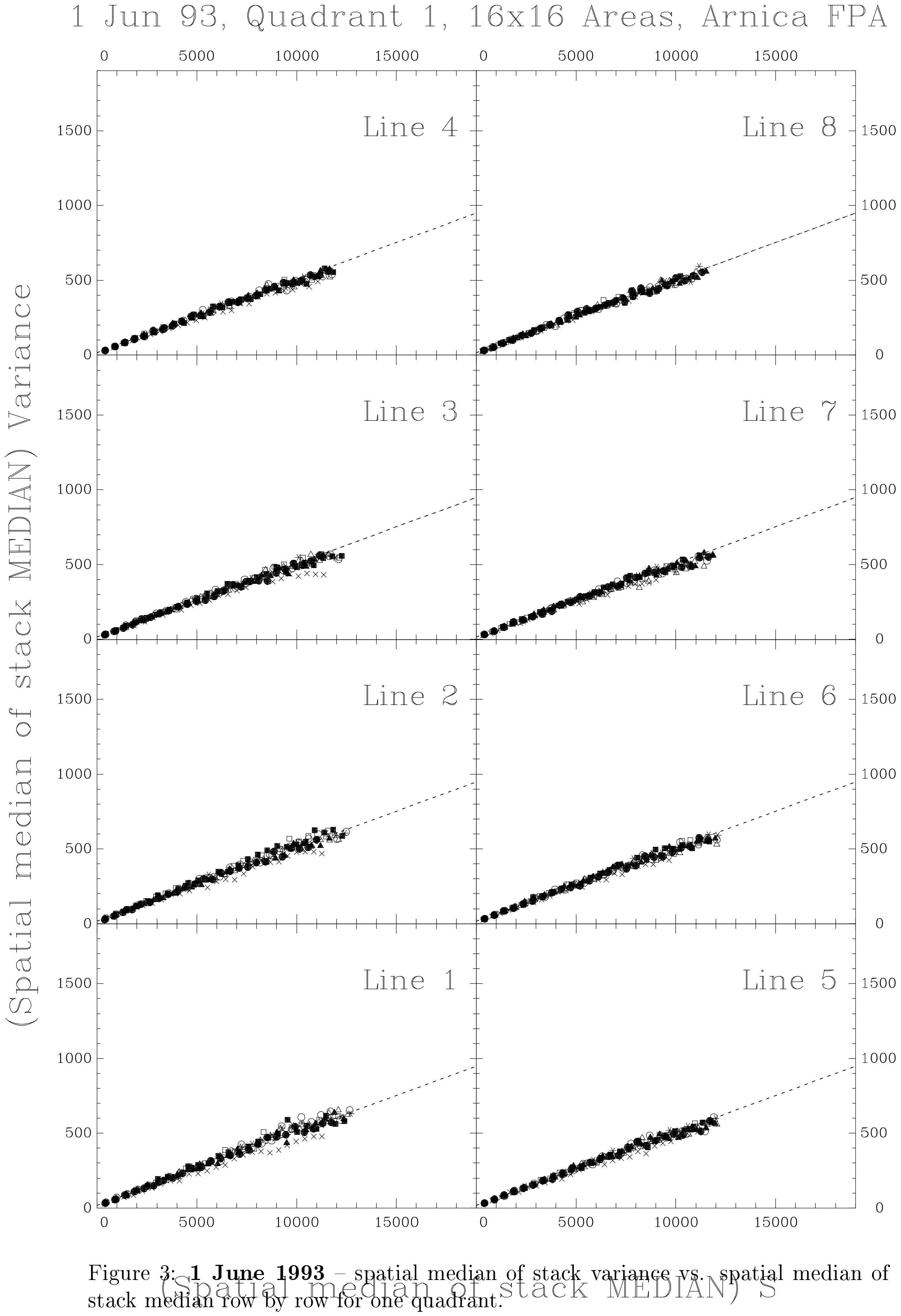


Figure 3: **1 June 1993** – spatial median of stack variance vs. spatial median of stack median row by row for one quadrant.

Table 2: Gain factor test results.

| Date | Code Name | $g$ [e$^-$/ADU] Quadrant | Average |
|---|---|---|---|
| 8 Dec 92[a] | Linear1 | 1 | 17.5 ± 6.7% |
| | | 2 | 20.0 ± 0.6% |
| | | 3 | 20.4 ± 1.6% |
| | | 4 | 19.2 ± 0.6% |
| | | All | **19.3 ± 6.7%** |
| 10 Dec 92[a] | Linear3 | 1 | 19.9 ± 0.6% |
| | | 2 | 20.0 ± 0.4% |
| | | 3 | 19.6 ± 0.4% |
| | | 4 | 19.7 ± 0.6% |
| | | All | **19.8 ± 0.9%** |
| 15 Mar 93[a] | Linear5 | 1 | 19.8 ± 0.4% |
| | | 2 | 20.2 ± 0.3% |
| | | 3 | 19.6 ± 0.3% |
| | | 4 | 19.8 ± 0.4% |
| | | All | **19.85 ± 1.1%** |
| 1 Jun 93[b] | Linear6 | 1 | 20.1 ± 0.4% |
| | | 2 | 19.9 ± 0.3% |
| | | 3 | 19.5 ± 0.3% |
| | | 4 | 19.7 ± 0.5% |
| | | All | **19.8 ± 1.4%** |
| 1 Jun 93[b] | Linear7 | 1 | 20.4 ± 0.4% |
| | | 2 | 20.4 ± 0.2% |
| | | 3 | 20.1 ± 0.2% |
| | | 4 | 20.2 ± 0.3% |
| | | All | **20.25 ± 0.9%** |
| 1 Jun 93[b] | Linear8 | 1 | 20.1 ± 0.4% |
| | | 2 | 20.1 ± 0.3% |
| | | 3 | 19.7 ± 0.2% |
| | | 4 | 19.9 ± 0.4% |
| | | All | **20.0 ± 1.0%** |
| 1 Jun 93[b] | Linear9 | 1 | 20.3 ± 0.4% |
| | | 2 | 20.3 ± 0.3% |
| | | 3 | 20.05 ± 0.2% |
| | | 4 | 20.2 ± 0.4% |
| | | All | **20.2 ± 0.6%** |

Notes to Table 2:
The last column in the table represents the inverse of the first-order coefficient of the linear fit, together with the error propagation of the formal error on the coefficient. When the average is a 4-quadrant average, denoted by "All", the error is the standard deviation of the four quadrants.

[a] Repeated $\forall i$: $[N_{\rm coadds} \times t_{\rm int}(i) + N_{\rm coadds} \times t_{\rm ref}]$.

[b] Repeated $\forall N_{\rm coadds}$: $\{\forall i : \quad [1 \times t_{\rm int}(i)]\}$.

Table 3: Read noise test results.

| Date | Source | $\sigma_r$ [e$^-$] | |
|---|---|---|---|
| | | Average | Fitted |
| Jun 92 | Dark(D) | 67 ± 6.0% | – |
| 28 Oct 92[a] | Dark(D) | 90 ± 10% | 80 ± 11% |
| 10 Dec 92[a] | Dark(D) | 45 ± 1.1% | 48 ± 1.7% |

Notes to Table 3:
[a] Repeated $\forall i$: $[N_{\rm coadds} \times t_{\rm int}(i) + N_{\rm coadds} \times t_{\rm ref}]$.
[b] Repeated $\forall N_{\rm coadds}$: $\{\forall i: \;\; [1 \times t_{\rm int}(i)]\}$.

## 5.2 Read noise

The images from a zero-flux source at a series of integration times were converted into the variance vs. signal representation as described in §4.2. The subareas were grouped into quadrants and a linear regression was performed on the spatial medians of the stack variance relative to the stack median. The results of these fits are presented in Table 3. Note that Col. 3 reports the *average* of the variance over the exposure time series, and Col. 4 reports the zeroth-order term of the linear fit (converted appropriately). Both quantities are the means from the four quadrants, and the quoted errors are standard deviations. Units are e$^-$, derived assuming a conversion factor of 20e$^-$/ADU.

A reliable estimate for the read noise for the ARNICA array is around 50 e$^-$ for double-correlated sampling (i.e., two reads of the detector)[3]. We have included in this estimate only the test of 10 Dec 92 because it is the only test of the dark current acquired with test data acquisition scheme *a*; estimates acquired with scheme *b* are from 2 to 3 times higher. Tests with illuminated sources (scheme *a*) give a fitted value for $\sigma_r$ of around 70 e$^-$, 30% higher than that implied from tests with the array shuttered down. Results from the acceptance testing in Tucson (June, 1992) are also given in Table 3. As can be seen from the Table, the October 1992 data were somewhat noisier than later data, as later hardware intervention on the detector electronics improved performance.

## 5.3 Dark current

The images from a zero-flux source at a series of integration times were fit pixel-by-pixel to a linear function of time, as described in §4.1. The medians of the first-order coefficient $a_1$ frames are given in Table 4. Units are e$^-$/s, derived assuming a conversion factor of 20e$^-$/ADU. Note that the October 1992 are omitted here, as there were only three data points for the pixel-by-pixel linear fit.

The array dark current + stray light for ARNICA can be *conservatively* estimated

[3]Dwell time for this estimate is 8$\mu$s, but this interval does not seem to significantly influence the noise properties of the measurements.

Table 4: Dark current test results.

| Date | Source | $a_1$ [e$^-$/s] Quadrant | Median |
|---|---|---|---|
| 10 Dec 92[a] | Dark(D) | All | 0.3 |

Notes to Table 4:
[a] Repeated $\forall i$: $[N_{\rm coadds} \times t_{\rm int}(i) + N_{\rm coadds} \times t_{\rm ref}]$.
[b] Repeated $\forall N_{\rm coadds}$: $\{\forall i : \ [1 \times t_{\rm int}(i)]\}$.

to be certainly $< 1$ e$^-$/s, and is probably $< 0.3$ e$^-$/s. Again, we include in this estimate only the result from the test taken with test data acquisition scheme $a$; estimates from tests acquired with scheme $b$ are from 3 to 10 times higher.

The low dark current in ARNICA makes subtraction of dark current unnecessary for typical broad-band applications. With a conversion factor of 20 e$^-$/ADU, even a 60 s on-chip integration time gives a dark current of $\sim$ 1ADU so that for broad-band imaging in which performance is background limited, subtraction of dark current frames only serves to introduces noise in the data.

## 5.4 Non-linearity

At the acceptance testing of ARNICA in June 1992, we discovered empirical evidence of the nonlinearity in NICMOS-3 devices. When different uniformly-illuminated scenes were used to flatfield one another, the high QE areas of the array tended to stand out in the flattened image. The effect was most pronounced when the illumination levels used for the flatfield correction were different by 50% or more. After careful testing and analysis (with the help of E. Mentzell of the University of Arizona Optical Sciences Laboratory), we concluded that the ARNICA array was not pathologically flawed and what we were observing was a manifestation of the inherent nonlinearity in NICMOS-3 devices.

We have analyzed the effects of nonlinearity by assuming a quadratic behavior for the output voltage described in §2. The intrinsic non-linearity in the array response (that is to say the amplitude of the second-order coefficient in a quadratic fit to the instrumental counts as a function of integration time) is roughly 1.5% for ADUs $\leq$ 13000. The simple treatment we have adopted here is adequate to linearize array output below levels of saturation (ADUs $\leq$ 15000) to $\leq$0.3%. A more sophisticated approach is given in McCaughrean (1988).

Consider the voltage output from the multiplexer as a function of the charge and the capacitance:

$$V(x,y) = \frac{q(x,y)}{C[q(x,y)]} = a_0 + a_1 q(x,y) + a_2 q^2(x,y)... \qquad (1)$$

where $q$ and $C$ are the charge and the capacitance of the individual multiplexer circuit, respectively. The coefficients $a_0$, $a_1$, and $a_2$ may also vary spatially. The output amplifier converts the multiplexer voltage to ADUs by a discrete, pseudo-linear process:

$$\begin{aligned} ADU(x,y) &= \frac{1}{g}V(x,y)C[q(x,y)] \\ &= b_0(x,y) + b_1(x,y)Ft\eta(x,y) + b_2(x,y)[Ft\eta(x,y)]^2 + ... \end{aligned} \tag{2}$$

where $\eta$ is the quantum efficiency of the array, $g$ is the gain conversion factor discussed in §5.1, and we have introduced an expression for the charge $q$ as the product of the impinging flux $F$, exposure time $t$, and $\eta$. $b_0$, $b_1$, and $b_2$ are the unknown polynomial coefficients equivalent to $a_0$, $a_1$, and $a_2$ rescaled. It can be seen that this model simplifies to an expression for the observed ADUs as a quadratic function of time.

The correction for non-linearity can now be easily calculated. The correct ADU level is just that part which is linear with integration time:

$$ADU_{\rm lin} = b_1(x,y)Ft\eta(x,y) \tag{3}$$

Therefore, we can substitute for $ADU_{\rm lin}$ in (2):

$$ADU = b_0 + ADU_{\rm lin} + \frac{b_2}{b_1^2}ADU_{\rm lin}^2 \tag{4}$$

and, solving for the quadratic gives an expression for the linear corrected counts in ADU as a function of the observed counts:

$$ADU_{\rm lin} = \frac{b_1^2}{2b_2}\left(-1 + \sqrt{1 + \frac{4b_2}{b_1^2}(ADU - b_0)}\right) \tag{5}$$

To calculate $b_0$, $b_1F\eta$, and $b_2F^2\eta^2$, we fit images from an illuminated source at a series of integration times pixel-by-pixel to a quadratic function of time as described in §4.1. The medians of the $b_0$ and the $b_2/b_1^2$ frames are given in Table 5.

It can be seen from the table that the correction factor, Col. 6, is relatively stable with time. The first two tests in December, 1992, and March, 1993 were acquired with a different acquisition scheme than that used in the later tests. We have found, on the basis of read noise and dark current analyses, that the first scheme is more reliable than the second. This could perhaps explain also the marked similarity between the correction factors derived from the two sets of measurements from December and March. The bias voltage applied when these these corrections were measured was 0.5 V.

We have applied Eqn. (5) to experimental data to correct for effects of non-linearity. Examples of this correction are shown in Fig.4. As stated before, the resulting ADU counts are linear to within 0.3% in the most non-linear parts of the detector. A procedure which applies this correction to data as the first step of data reduction has been developed, and is part of the ARNICA data reduction package

Table 5: Non-linearity test results.

| Date | Code Name | [ADU] $b_0$ | [ADU s$^{-1}$] $b_1 F\eta$ | [ADU s$^{-2}$] $b_2 F^2\eta^2$ | $\times 10^{-6}$ $b_2/b_1^2$ |
|---|---|---|---|---|---|
| (1) | (2) | (3) | (4) | (5) | (6) |
| 10 Dec 92[a] | Linear3 | -148.5 ( 9) | 913.4 (185) | -2.2 ( 7) | 2.7 |
| 15 Mar 93[a] | Linear5 | -78.4 (14) | 443.4 (439) | -0.5 (15) | 2.7 |
| 1 Jun 93[b] | Linear6 | -90.8 (17) | 546.8 (485) | -1.0 (22) | 3.4 |
| 1 Jun 93[b] | Linear7 | -75.2 (17) | 444.7 (559) | -0.6 (22) | 3.2 |
| 1 Jun 93[b] | Linear8 | -43.7 | 283.5 | -0.2 | 3.1 |
| 1 Jun 93[b] | Linear9 | -50.8 (10) | 311.1 (472) | -0.3 (19) | 3.3 |

Notes to Table 5:
Cols. (3) – (6): Medians of frames from pixel-by-pixel quadratic fit. The values in parentheses are the median values of the signal-to-noise frames obtained by propagating the errors in the quadratic fit.
[a] Repeated $\forall i$: $[N_{\mathrm{coadds}} \times t_{\mathrm{int}}(i) + N_{\mathrm{coadds}} \times t_{\mathrm{ref}}]$.
[b] Repeated $\forall N_{\mathrm{coadds}}$: $\{\forall i: \quad [1 \times t_{\mathrm{int}}(i)]\}$.

to be described in the third report of this series. We note that applying a scalar correction (i.e., one that does not depend on position) for non-linearity was not as effective as the frame correction, as the spatial variations in the second-order fits are too large.

## 5.5 Cosmetic quality and bad pixel correction

The tests with illuminated sources were used to derive the bad pixel mask. Although we tried different approaches, the one we consider the most reliable for accurate quantitative results, is the following[4]. We first created a high signal-to-noise image of a spatially uniform source. This image was then subjected to a spatial median filter with a 5×5 smoothing window. The 5-pixel smoothing window is a compromise between bad pixel cluster size and typical spatial structure in the array QE; larger bad pixel clusters require larger smoothing windows for detection. The smoothed image was then subtracted from the original to yield a spiky (both positive and negative) flat image with zero median. We defined bad pixels as those which fell outside the $\pm 5\sigma$ range in the histogram of the difference image. A typical histogram is shown in Fig. 5.

The next step was to unite possible clusters of bad pixels, so as to make possible a linear interpolation around the corrupted area. This was done manually from the bad pixel list, and checked visually with a mask image. The numbers of bad pixels are given in Table 6. Note that the third column lists the total number of bad pixels, grouped into contiguous rectangular regions (i.e., "clusters"), to be corrected

[4] We also considered, for example, the first-order coefficient in the fit for the non-linearity correction, or the same for the dark current.

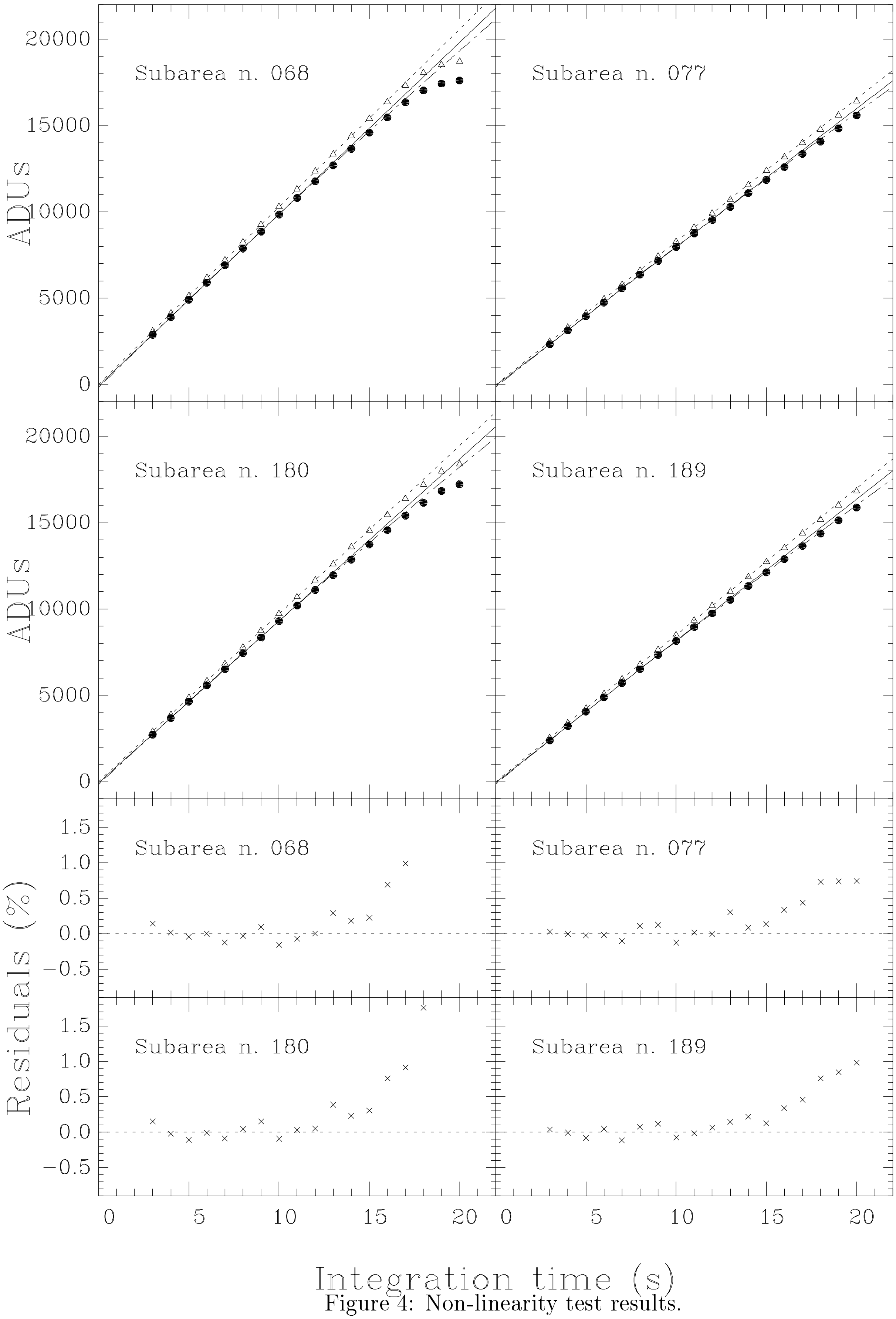


Figure 4: Non-linearity test results.

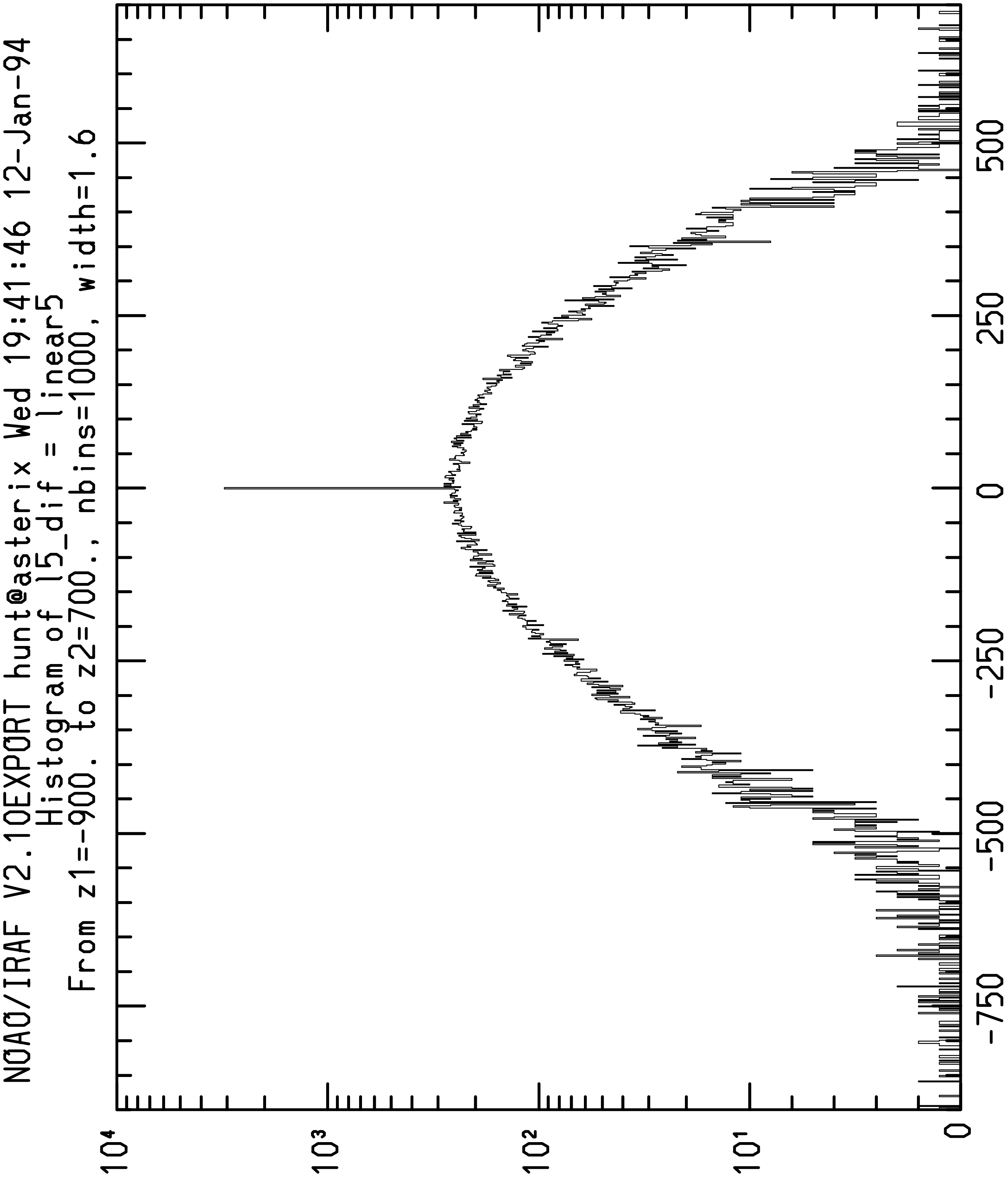


Figure 5: Histogram of difference image after smoothing and subtraction.

Table 6: Bad pixel statistics.

| Date | Individuals | Clusters |
|---|---|---|
| 10 Dec 92 | 437 | 597 |
| | (0.67%) | (0.91%) |
| 15 Mar 93 | 516 | 726 |
| | (0.79%) | (1.1%) |
| 1 Jun 93 | 580 | 852 |
| | (0.89%) | (1.3%) |

by linear interpolation. The bad pixel lists and masks derived here are incorporated in the ARNICA data reduction package to be described in the third report of this series.

The method outlined above for flagging the bad pixels in the detector is somewhat more severe than methods typically used for industry specifications. Pixel quality of a scientific grade NICMOS-3 array is characterized by the manufacturer in terms of the number of pixels that have a QE $>$ 50% of the mean QE. The number of pixels that did not satisfy such a criterion for the array in ARNICA, as quoted by Rockwell in March, 1992, was 363 pixels or 0.55%. In December, 1992, we find 0.67% of the pixels present deviant behavior and were defined by our procedure to be "bad". This difference is almost certainly due to the severity of our definition of bad pixels.

Behavior of bad pixels in NICMOS-3 arrays seems to be characterized by gradual degradation with time that is probably associated with detector thermal cycling. Clusters of bad pixels seem to get larger with time, and the early bad pixel lists tend to be subsets of later ones. Applying the same technique to the sets of tests in December, March, and June, we detect 18% more bad pixels in March than December, and 12% more in June than in March. When these are combined into clusters (third column in Table 6), the difference between March and December is 20%, and the difference between June and March is 17%.

Detection of bad pixels and their behavior also seems to depend on the flux level of the images used to for the detection. This implies that careful elimination of all the unreliable pixels in a given image requires detailed manual intervention. We also note that the automated method described here is not always effective for flagging those pixels with sporadic anomalous behavior; again such pixels are better determined by hand and eye from the individual images to be corrected.

# 6 Conclusions

We have presented here methods for evaluating parameters of a two-dimensional focal plane array. Results obtained show that the NICMOS-3 array detector installed in ARNICA conforms to the specifications for a scientific grade focal plane array.

Table 7: ARNICA detector parameters.

| Parameter | Value |
|---|---|
| $g$ | 20.0 [$e^-$/ADU] |
| $\sigma_r$ | 50 [$e^-$] |
| Dark current | $\leq 0.5$ [$e^-$/s] |
| Non-linearity | $3 \times 10^{-6}$ |
| Bad pixels | 0.7–0.9% |

Moreover, characteristics of the detector+electronics such as conversion factor, read noise, dark current, and non-linearity appear to be stable with time. Table 7 gives estimates of the detector parameters discussed in this report.

## References

Baffa, C. 1991, Arcetri Technical Report No. 11/1991

Fowler, A.M. and Gatley, I. 1990, ApJ, 353, L33

Lisi, F. 1991, Arcetri Technical Report No. 16/1991

Lisi, F., Baffa, C., and Hunt, L. 1993, "ARNICA: the Arcetri Observatory NICMOS-3 imaging camera", Proceedings of SPIE Technical Conference 1946, Orlando

Mackay, C.D. 1986, Annual Review of Astronomy and Astrophysics, 24, 255

McCaughrean, M.J. 1988, Ph.D. Thesis, University of Edinburgh

McLean, I.S. 1988, *Electronic and Computer-Aided Astronomy: From Eyes to Electronic Sensors*, John Wiley & Sons, Chichester